RSC Advances

ROYAL SOCIETY OF CHEMISTRY

www.rsc.org/advances

Tuning electronic and magnetic properties of zigzag graphene nanoribbons with a Stone-Wales line defect by positions and axis tensile strain

W. X. Zhang [1], C. He[2, *], T. Li [1], S. B. Gong [1]

[1]School of Materials Science and Engineering, Chang'an University, Xi'an 710064, China

[2]State Key Laboratory for Mechanical Behavior of Materials, School of Materials Science and Engineering, Xi'an Jiaotong University, Xi'an 710049, China

Abstract

In this paper, the electronic and magnetic properties of zigzag graphene nanoribbon (ZGNR) with a Stone-Wales line defect (SW LD) under axis tensile have been investigated by density functional theory. The calculation results reveal that the axis tensile and the position of SW LD significantly affect the electronic and magnetic properties of ZGNRs. In the unstrained systems, the SW LD is more stable near the edge, and the antiferromagnetic (AFM) semiconductors have indirect band gaps (E_g). With the increasing tensile ε, E_g values of all the AFM semiconducting systems gradually decrease. Moreover, by shifting SW LD from the center to the edge or increasing tensile ε, Semiconductor → Half-metal → Metal transition with antiferromagnetic → ferromagnetic transfer can be achieved for the systems. The diverse and tunable electronic and magnetic properties enlarge defective ZGNRs potential applications in electronics and spintronics.

* Corresponding Author: C. He; E-mail address: hecheng@mail.xjtu.edu.cn

1. Introduction

Graphene consists of a hexagonal monolayer network of sp^2-hybridized carbon atoms. When single-layers of graphene were isolated for the first time by mechanical exfoliation,[1] the subsequent discovery of its unusual electronic and magnetic properties had led to an extraordinary amount of interest and promised variety of applications.[2-5] In addition to some early works,[6, 7] possibility of very large one-atom-thick 2D crystals is reported theoretically[8-10] and experimentally,[11] especially after large-scale synthesis methods like chemical vapor-deposition[12 ,13] and epitaxial growth[14, 15] on metal and SiC substrates are developed.

Not only extended 2D graphene-like nanosheets but also quasi-one-dimensional (1D) graphene nanoribbons (GNRs) with armchair or zigzag edges have shown unusual electronic,[16-24] magnetic,[21-26] and quantum-transport properties.[27-29] A general method to properly modulating the electronic properties of graphene and GNRs at nanoscale is chemical functionalization or doping, which has been widely investigated using various techniques.[21-23, 30-32] Like in other materials, structural defects do exist in graphene and can also be deliberately introduced into the host graphene lattice to dramatically alter its properties by irradiation or chemical treatments.[9,10, 33-36] One of the unique properties is that the graphene lattice could reconstruct by forming nonhexagonal rings, which may either introduce curvature in the sheet or leave it flat when the arrangement of polygons satisfies certain symmetry rules. Furthermore, transmission electron microscopy (TEM)[37-39] and scanning tunneling microscopy (STM)[40, 41] have proven the occurrence of either native or physically introduced defects in graphene by obtaining images of nonhexagonal rings at atomic scale.

Stone et. al have reported that the Stone-Wales defect (SW), which four hexagons are transformed into two pentagons and two heptagons by rotating one of the C-C bonds by 90°, does not involve any removed or added atoms.[42] The defected structure retains the same number of atoms as perfect graphene, and no dangling bonds are introduced. In graphene, the concept of zero-dimensional point defects is quite similar to bulk crystals, but line defects already play a different role.[39] It is well-known that defects are not always stationary and that their migration can have an important influence on the properties of a defective crystal. In graphene, each defect has certain mobility parallel to the graphene plane. Generally, the line defects (LD) are tilt boundaries separating two domains of different lattice orientations with the tilt axis normal to the plane, which can be thought of as a line of reconstructed point defects with or without dangling bonds[10, 39, 42] Lahiri et. al have observed a domain boundary due to lattice mismatch in graphene grown on a Ni surface.[34] Banhart et. al have addressed that the linear defect corresponding to grain boundaries in graphene should be of paramount importance and grain boundaries may govern the electronic transport in such samples.[42] Furthermore, when the linear array of defect are embedded in armchair-GNRs (AGNRs) and zigzag-GNRs (ZGNRs), the hybrid GNRs could exhibit unique electronic and transport properties that differ from the perfect AGNRs and ZGNRs.[10, 39] Yet a detailed theoretical understanding of electronic and magnetic properties of these Stone-Wales line defects (SW LD) embedded in ZGNRs remains unclear.

On the other hand, mechanical strain could affect the electronic properties of graphene due to being grown on different substrates and thus have significant impact on their device applications.[43-45] Ferralis et. al. have reported that the band gap of AGNRs can change in a

zigzag manner under uniaxial strain,[45] which shed light on a flexible approach to fabricate electromechanical devices with graphene-like materials.

Therefore, in this paper, the effects of the position of SW LD on the structural, electronic and magnetic properties of ZGNRs are comprehensively carried out by density functional theory (DFT). Meanwhile, the influences of the defect location on these properties under tensile strain (ε) have also been considered. These studies provide us a deep understanding of the novel properties of defective ZGNRs, which is essential to enrich them for future nanodevices.

2. Computational methods

The simulations are based on density functional theory (DFT), which is provided by DMOL^3.[46-48] The generalized gradient approximation (GGA) with the Perdew - Burke - Ernzerhof scheme (PBE) [49] is adopted for the exchange-correlation potential to optimize geometrical structures and calculate properties for both spin-polarized and spin-unpolarized case.[49] Similar functional has been successfully used to study the structural and electronic properties of GNRs, water, Si and Cu nanowires.[2, 9, 23, 50, 51] The All-Electron Relativistic Kohn-Sham wave functions (AER) and double numeric plus polarization (DNP) basis set are adopted in the local atomic orbital basis set for DMOL^3.[46] The Brillouin zone is sampled by 1 × 8 × 1 (1 × 10 × 1) *k*-points for all structures in the geometry optimization (electronic) calculations, which brings out the convergence tolerance of energy of 1.0×10^{-5} Ha (1 Ha = 27.2114 eV), maximum force of 0.002 Ha/Å, and maximum displacement of 0.005 Å.[50-52] Based on the optimized structures, the axis tensile ε along the ZGNRs axis direction is modulated by the corresponding lattice parameters.[51, 53] For geometry optimization, both the

cell and the atomic positions are allowed to fully relax to find the equilibrium states. Periodic boundary conditions are adopted for all utilized models in this work. To ensure that the interactions between the defective ZGNR in neighboring cells, the vacuum of greater than 15 Å is added both to neighboring cells and along the width direction. All electronic and magnetic properties of the systems are calculated in their ground states, which are identified by comparing the energies of nonmagnetic state (NM), ferromagnetic coupling (FM), and antiferromagnetic coupling (AFM). The one with the lowest energy is the ground state.

3. Results and discussion

In our simulation, ZGNRs with $W = 10$ (10-ZGNRs) are analyzed, where the nanoribbon width (W) is defined by the number of zigzag chains perpendicular to the axial direction. For 10-ZGNRs with SW LD, two pentagons and two heptagons [SW defect] are symmetrically arranged along the nanoribbon axial direction, which are shown in Fig. 1a-e. As shown in Fig. 1a, when the C-C dimer lines are replaced by SW defect at the middle part of the 10-ZGNR (4 zigzag chains on both sides of C-C dimer lines), SW LD locates at the center of ZGNR. Thus, this kind of defective ZGNR can be considered as two ZGNR parts connected by C-C dimer lines. The structure of Fig. 1b-e are constructed by gradually moving the position of SW LD along the C-C dimer lines from the center to the left edge of 10-ZGNR. Here the systems of 10-ZGNRs with SW LD are named as *n*-SW-*m*, where *n* and *m* are the number of zigzag chains on the left and right sides of the C-C dimer lines, respectively. The dangling bonds at both edges are saturated by hydrogen atoms for all systems.

In order to study the preferred coupling of these moments, we have calculated the energies of NM, FM, and AFM for the 4-SW-4, 3-SW-5, 2-SW-6, 1-SW-7, and 0-SW-8

systems, respectively. The calculated energies of the AFM state for 4-SW-4, 3-SW-5, 2-SW-6, and 1-SW-7 systems are comparatively lower than those of the FM and NM states, respectively. Thus, the ground state in these systems is the AFM state. While for 0-SW-8 system, the FM state is more energetically favorable. The results demonstrate that when SW LD is introduced, the position of SW LD has a great effect on the magnetic configurations of the *n*-SW-*m* systems. As SW LD moves from the center to the left edge, the systems experience a transition from AFM to FM state.

Once the ground states have been confirmed, the relative stability of these *n*-SW-*m* systems is subsequently investigated to search the most stable structure. Their total energies by choosing the energy of 4-SW-4 system as a reference are shown in Fig. 1f. The results show that the total energies of the *n*-SW-*m* systems become more and more negative and thus the system is increasingly stable as SW LD shifts away from the center. Especially, there is a large drop in energy from 2-SW-6 to 0-SW-8 system, which indicates that SW LD near the edge is more favorable.

Fig. 2a-e displays the spin-polarized band structures of the five *n*-SW-*m* systems. It can be seen that the band structures of *n*-SW-*m* systems vary with the different locations of SW (55-77) LD in ZGNRs. The energy bands of 4-SW-4 system for both spins are degenerate, while for other *n*-SW-*m* systems, the energy bands near the E_f split into two subbands (spin up and spin down) and exhibit some deformation. When SW LD shifts away from the center, the degree of splitting and deformation becomes stronger. The band gap of *n*-SW-*m* systems is defined by the energy difference between the conduction band minimum (CBM) and the valence band maximum (VBM), i.e., E_g = CBM - VBM. CBM and VBM are each

characterized by a certain crystal momentum (*k*-vector) in the Brillouin zone.[53] As shown in Fig. 2 a-c, because the *k*-vector of CBM and VBM are different, the three systems of 4-SW-4, 3-SW-5, and 2-SW-6 are semiconductors with indirect E_g. As SW LD moves gradually to the left edge, E_g values for the three semiconductors decrease gradually and the corresponding E_g values of each semiconducting *n*-SW-*m* systems are 0.297 eV, 0.217 eV 0.054 eV, respectively. Compared with our calculated E_g value of 0.38 eV for perfect 10-ZGNR, E_g values of these three semiconducting systems decrease because the impurity states near the E_f is induced by the SW LD. When SW LD appears near the edge in the other two systems (1-SW-7 and 0-SW-8), the electronic properties exhibit unusual features differing from the semiconducting characteristic. In Fig. 2d, the 1-SW-7 system exhibits a half-metallic character, where the spin up and down states respectively show the semiconducting and metallic behaviors. While for the 0-SW-8 system in Fig. 2e, there is no E_g opening for both spin up and down states, which displays a distinguished metallic behavior. In addition, compared with other *n*-SW-*m* systems, the energy bands of the 0-SW-8 dramatically change near the E_f.

Next we studied the influences of axis tensile ε on the electronic properties of these *n*-SW-*m* systems. For the semiconducting systems, the axis tensile ε always reduces E_g to zero rapidly, where a transition from semiconductor to half-metal appears. The corresponding ε_c values for the electronic transition (semiconductor → half-metal) are 2.5, 2.0, and 1.2% for 4-SW-4, 3-SW-5, and 2-SW-6 systems, respectively. Further increasing axis tensile ε, the transition from AFM half-metallic to FM metals of the three systems will occur quickly. The spin-polarized band structures of the three semiconducting systems are calculated to better

understand the effects of axis tensile ε on the electronic properties, which are shown in Fig. 3. With increasing of axis tensile ε, the electronic distributions of the bands near the E_f become apparently asymmetric between the spin up and down bands. When the three systems become AFM half-metals, the spin up and down channels show semiconducting and metallic behaviors, respectively, as shown in Fig. 3. As ε further increases to the critical transition values (AFM half-metallic to FM metals) for each system, the bands near the E_f experience stronger spin splitting in Fig. 4.

Moreover, in order to deeply describe the electronic structure of *n*-SW-*m* systems, the corresponding electronic distributions at the Gamma point have been explored. For the three semiconducting systems (4-SW-4, 3-SW-5, and 2-SW-6) and the half-metallic system (1-SW-7), the electronic distributions of bands display similar behaviors. Thus, taken the system 3-SW-5 as an example (in Fig. 4a), the highest occupied molecular orbital (HOMO) is mainly localized on the edge C atoms, and the lowest unoccupied molecular orbital (LUMO) is primarily localized on the defect C atoms, where E_g of this system is determined by the two subbands. More interestingly, for HOMO – 4 (the fourth orbital under HOMO), the electronic states mainly distribute on the left edge and defect site, which indicates that a strong interaction exists between the left edge and defect site due to serious deformation as SW LD moves to the left edge. Meanwhile LUMO + 4 (the fourth orbital up LUMO) are completely localized on the right edge of defective ZGNR. Both of the electronic distribution for HOMO – 4 and LUMO + 4 also distribute along C−C bonds.

According to the total density of states (DOS) and Partial DOS for 3-SW-5 system in Fig. 4b, the electronic states near the E_f are determined by both the defect C atoms and the two

edges of ZGNR, which are corresponding to the former results that the impurity states appear near the E_f. The results of calculated ground states and the Partial DOS demonstrate that SW LD introduces impurity states within E_g of the perfect ZGNR, thus leading to the reduction of E_g for the semiconducting 4-SW-4, 3-SW-5, and 2-SW-6 systems.

While for the metallic 0-SW-8 system in Fig. 4c, the HOMO orbital is only localized on the right edge of ZGNR, and LUMO orbital distributes on the defect sites. The HOMO – 4 and LUMO + 4 charge densities are mainly centered at single C atoms. However, the densities are inhomogeneous over the whole region.

Meanwhile, HOMO-4, HOMO, LUMO and LUMO+4 for 3-SW-5 with ε = 5.0% are shown in Fig. 4d for comparison. For the system 3-SW-5 at FM state, the HOMO orbital is mainly localized on the right edge C atoms, and the LUMO orbital is completely contributed by the defect C atoms. For HOMO – 4, the electronic states mainly distribute on the left edge and defect sites along the periodic direction, while LUMO + 4 are localized along C−C bonds in unaxis direction.

The results of magnetic properties for these *n*-SW-*m* systems are shown in Fig. 5. As shown in Figs. 5a and b, for the systems 4-SW-4 and 3-SW-5, the two edges of ZGNR are still antiferromagnetically coupled, and the magnetism on the atoms connected to the C-C dimers are also antiferromagnetically aligned. Because the ZGNR with SW LD could be considered as a combination of two ZGNR parts aligned C-C dimers, the atoms connected with the C-C dimers are antiferromagnetically coupled, which is similar to the case of perfect ZGNRs. Meanwhile, the half-metallic system and the semiconducting systems exhibit a similar magnetic ordering and their rest magnetic moments are zero. However, for the

metallic system 0-SW-8 (Fig. 5c), the ground state is FM, and the magnetic alignment on the two edges of the system become FM ordering, which resulting in a net magnetic moment of 1.17 μB. This clearly indicates that the magnetic moment is mainly contributed by C atoms on the right edge.

Considering the symmetrical characteristic of SW LD, the similar effect of the defect location on the electronic and magnetic properties could be drawn as SW LD moved to the right edge.

Similarly, the magnetic properties of these *n*-SW-*m* systems with or without axis tensile ε on are also discussed here. The energy difference ΔE between E_{FM} and E_{AFM} of *n*-SW-*m* systems has also been calculated. For the half-metallic 1-SW-7 system in the unstrained case, the ground state favors AFM configuration. When $\varepsilon \geq 1.5\%$, the system changes into the FM state. Further increasing ε, the metallic system 0-SW-8 does not change the FM ground state and still remains FM configuration, even though the initial spin configuration is set as the AFM state. For the three semiconducting systems (4-SW-4, 3-SW-5, and 2-SW-6), when ε = 0, $\Delta E > 0$ and their ground states are AFM configurations, which are discussed above. As ε increases, ΔE decreases gradually. Then, at the critical ε (ε_c) of 2.8, 2.6, and 1.9%, the AFM → FM transitions take place with $\Delta E < 0$ for the three systems, respectively. And it is clear that ε_c for this magnetic transition decreases gradually as SW LD shifts away from the center. Further increasing axis tensile ε will lead to the ΔE more negative, which indicates that the FM states for these systems become more stable. Moreover, for the three semiconducting systems, the magnetic alignments on the edges and the defect site under ε are similar. The spin density distributions ($\Delta\rho = \rho_{up} - \rho_{down}$) for 3-SW-5 under different strain (the axis tensile ε

= 1.0, 3.0, and 5.0%) are shown in Fig. 6. At the AFM state (ε = 1.0%), the spin ordering is antiferromagnetically coupled between the two edges, but ferromagnetically coupled along the C atoms connected to the C-C dimers. And the total magnetic moment is little. With the increasing axis tensile ε, when $\varepsilon \geq \varepsilon_c$, the magnetic configuration of the system becomes FM state, in which the magnetic coupling between the two edges changes from antiparallel to parallel. Moreover, the spin densities on the two edges and SW LD increase with increasing ε, which is consistent with the enhanced stability of the FM state. The situation for other semiconducting systems 4-SW-4 and 2-SW-6 is similar.

The total magnetic moments of all the *n*-SW-*m* systems under ε are also studied. The calculated results demonstrate that the magnetism is mainly contributed by the two edges and SW LD. As ε increases, the total magnetic moments of these systems change from 0.72 to 2.1 μB and the magnetic moments on the two sites increase slowly.

Finally, we summarize the computed properties for *n*-SW-*m* versus axis tensile ε in Fig. 7. Clearly, the intriguing and diverse transformation in electronic and magnetic properties of the novel SW LD systems remarkably depends on line defect sites. As SW LD moves from the center to the edge, in the unstrained systems, Semiconductor → Half-metal → Metal (AFM → FM) transitions can be achieved. Under axis tensile ε, E_g values of all the semiconducting systems decrease gradually. The critical transition ε values of each system are also shown in Fig. 7. Our results predict that effectively controlling the LD sites is a tunable way to modulate the electronic and magnetic properties of ZGNRs.

4. Conclusions

In summary, we have investigated the modulation of structural, electronic and magnetic

properties through changing the SW LD locations and axis tensile of 10-ZGNRs by density functional theory. In the unstrained systems, SW LD is more stable near the edge, and AFM semiconductors have indirect band gaps. As SW LD moves from the center to the edge, a Semiconductor → Half-metal → Metal (AFM → FM) transition can be achieved. With the increasing tensile ε, E_g values of all the AFM semiconducting systems gradually decrease and AFM Semiconductor → AFM Half-metal → FM Metal transitions also occur for each system. These diverse properties are of fundamental significance and open up exciting opportunities for the design of novel nanoelectronic spintronic devices.

Acknowledgements

The authors acknowledge supports by National Natural Science Foundation of China (NSFC, Nos. 51177006, 51301020 and 51471124), Natural Science Foundation of Shaanxi province, China (2014JQ6196), Ph.D. Programs Foundation of Ministry of Education of China (Grant No. 20110201120002), the special fund for basic scientific research of central colleges of Chang'an University (No. 2013G1311053) and State Key Laboratory for Mechanical Behavior of Materials.

References

1. K. S. Novoselov, A. K. Geim, S. V. Morozov, D. Jiang, Y. Zhang, S. V. Dubonos, I. V. Grigorieva, and A. A. Firsov, *Science*, 2004, **306**, 666.
2. Q. G. Jiang, Z. M. Ao, S. Li and Z. Wen, *RSC Adv.*, 2014, **4**, 20290.
3. A. W. Robertson, C. S. Allen, Y. A. Wu, K. He, J. Olivier, J. Neethling, A. I. Kirkland and J. H. Warner, *Nat. Commun.*, 2012, **3**, 1144.
4. R. R. Nair, I. L. Tsai, M. Sepioni, O. Lehtinen, J. Keinonen, A. V. Krasheninnikov, A. H. Castro Neto, M. I. Katsnelson, A. K. Geim and I. V. Grigorieva, *Nat. Commun.*, 2013, **4**, 2010.
5. W. Gao, J. E. Mueller, J. Anton, Q. Jiang and T. Jacob, *Angew. Chem., Int. Ed.*, 2013, **52**, 14237.
6. N. D. Mermin, *Phys. Rev.*, 1968, **176**, 250.
7. P. Le Doussal and L. Radzihovsky, *Phys. Rev. Lett.*, 1992, **69**, 1209.
8. A. Fasolino, J. H. Los, and M. I. Katsnelson, *Nature Mater.*, 2007, **6**, 858.
9. M. Baldoni, A. Sgamellotti, and F. Mercuri, *Chem. Phys. Lett.*, 2008, **464**, 202.
10. Q. Q. Dai, Y. F. Zhu and Q. Jiang, *J. Phys. Chem. C*, 2013, **117**, 4791.
11. J. C. Meyer, A. K. Geim, and M. I. Katsnelson, *Nature*, 2007, **446**, 60.
12. S. Bae, H. Kim, Y. Lee, X. Xu, J. S. Park, Y. Zheng, J. Balakrishnan, T. Lei, H. R. Kim, Y. I. Song, Y. J. Kim, K. S. Kim, B. Ozyilmaz, J. H. Ahn, B. H. Hong, and S. Iijima, *Nat. Nanotechnol.*, 2010, **5**, 574.
13. K. S. Kim, Y. Zhao, H. Jang, S. Y. Lee, J. M. Kim, K. S. Kim, J. H. Ahn, P. Kim, J. Y. Choi, B. H. Hong, *Nature*, 2009, **457**, 706.
14. C. Berger, Z. Song, T. Li, X. Li, A. Y. Ogbazghi, R. Feng, Z. Dai, A. N. Marchenkov, E. H. Conrad, P. N. First, and W. A. de Heer, J. *Phys. Chem. B*, 2004, **108**, 19912.
15. C. Berger, Z. Song, X. Li, X. Wu, N. Brown, C. Naud, D. Mayou, T. Li, J. Hass, A. N. Marchenkov, E. H. Conrad, P. N. First, and W. A. de Heer, *Science*, 2006, **312**, 1191.
16. Y. W. Son, M. L. Cohen, and S. G. Louie, *Phys. Rev. Lett.*, 2006, **97**, 216803.
17. V. Barone, O. Hod, and G. E. Scuseria, *Nano Lett.*, 2006, **6**, 2748.
18. D. A. Areshkin, D. Gunlycke, and C. T. White, *Nano Lett.*, 2007, **7**, 204.
19. M. Ezawa, *Phys. Rev. B*, 2006, **73**, 045432.

20. F. J. Martín-Martínez, S. Fias, G. Van Lier, F. De Proft, and P. Geerlings, *Chem.-Eur. J.*, 2012, **18**, 6183.
21. F. J. Martín-Martínez, S. Fias, G. Van Lier, F. De Proft, and P. Geerlings, *Phys. Chem. Chem. Phys.*, 2013, **15**, 12637.
22. P. Wagner, C. P. Ewels, V. V. Ivanovskaya, P. R. Briddon, A. Pateau, and B. Humbert, *Phys. Rev. B*, 2011, **84**, 134110.
23. T. Wassmann, A. P. Seitsonen, A. M. Saitta, M. Lazzeri, and F. Mauri, *J. Am. Chem. Soc.*, 2010, **132**, 3440.
24. T. Wassmann, A. P. Seitsonen, A. M. Saitta, M. Lazzeri, and F. Mauri, *Phys. Rev. Lett.*, 2008, **101**, 096402.
25. K. Kobayashi, *Phys. Rev. B*, 1993, **48**, 1757.
26. K. Nakada, M. Fujita, G. Dresselhaus, and M. S. Dresselhaus, *Phys. Rev. B* 1996, **54**, 17954.
27. Y. W. Son, M. L. Cohen, and S. G. Louie, *Nature*, 2006, **444**, 347.
28. M. Topsakal, H. Sevinçli, and S. Ciraci, *Appl. Phys. Lett.*, 2008, **92**, 173118.
29. J. Y. Yan, P. Zhang, B. Sun, H. Z. Lu, Z. Wang, S. Duan, and X. G. Zhao, *Phys. Rev. B*, 2009, **79**, 115403.
30. S. Kattel, P. Atanassov, and B. Kiefer, *J. Phys. Chem. C*, 2012, **116**, 8161.
31. E. J. Kan, Z. Y. Li, J. L. Yang, and J. G. Hou, *J. Am. Chem. Soc.*, 2008, **130**, 4224.
32. H. J. Xiang, E. J. Kan, S. H. Wei, M. H. Whangbo, and J. L. Yang, *Nano Lett.*, 2009, **9**, 4025.
33. A. W. Tsen, L. Brown, M. P. Levendorf, F. Ghahari, P. Y. Huang, R. W. Havener, C. S. Ruiz-Vargas, D. A. Muller, P. Kim and J. Park, *Science*, 2012, **336**, 1143.
34. J. Lahiri, Y. Lin, P. Bozkurt, I. I. Oleynik and M. Batzill, *Nat. Nanotechnol.*, 2010, 5, 326.
35. A. W. Robertson, C. S. Allen, Y. A. Wu, K. He, J. Olivier, J. Neethling, A. I. Kirkland and J. H. Warner, *Nat. Commun.*, 2012, **3**, 1144.
36. C. Q. Sun, Y. G. Nie, J. S. Pan, X. Zhang, S. Z. Ma, Y. Wang and W. T. Zheng, *RSC Adv.*, 2012, **2**, 2377.
37. K. Kim, Z. Lee, W. Regan, C. Kisielowski, M. F. Crommie and A. Zettl, *ACS Nano*, 2011,

5, 2142.

38. J. C. Meyer, C. Kisielowski, R. Erni, M. D. Rossell, M. F. Crommie, A. Zettl, *Nano Lett.*, 2008, **8**, 3582.
39. F. Banhart, J. Kotakoski, and A. V. Krasheninnikov, *ACS Nano*, 2011, **5**, 26.
40. M. M. Ugeda, I. Brihuega, F. Guinea, and J. M. GÓmez-Rodríguez, *Phys. Rev. Lett.*, 2010, **104**, 096804.
41. A. J. Stone, and D. J. Wales, *Chem. Phys. Lett.* 1986, **128**, 501.
42. O. V. Yazyev, and S. G. Louie, *Phys. Rev. B*, 2010, **81**, 195420.
43. Y. Zhang, X. J. Wu, Q. X. Li, and J. L. Yang, *J. Phys. Chem. C*, 2012, **116**, 9356.
44. C. He, W. X. Zhang, Z. Q. Shi, J. P. Wang, and H. Pan, *Appl. Phys. Lett.*, 2012, **100**, 123107.
45. N. Ferralis, R. Maboudian, and C. Carraro, *Phys. Rev. Lett.*, 2008, **101**, 156801.
46. H. Y. He, J. Hu, and B. C. Pan, *J. Chem. Phys.* 2009, **130**, 204516.
47. C. He, W. X. Zhang, and J. L. Deng, *J. Phys. Chem. C*, 2011, **115**, 3327.
48. B. Delley, *J. Chem. Phys.* 1990, **92**, 508.
49. J. P. Perdew, K. Burke, and M. Ernzerhof, *Phys. Rev. Lett.* 1996, **77**, 3865.
50. R. G. Zhang, G. R. Wang, B. J. Wang, L. X. Ling, *J. Phys. Chem. C* 2014, **118**, 5243.
51. C. He, P. Zhang, Y. F. Zhu, and Q. Jiang, *J. Phys. Chem. C* 2008, **112**, 9045.
52. R. G. Zhang, G. R. Wang, B. J. Wang, L. X. Ling, *J. Phys. Chem. C* 2014, **118**, 5243.
53. S. Li, Q. Jiang, and G. W. Yang, *Appl. Phys. Lett.*, 2010, **96**, 213101.

Captions

Fig. 1 (a-e) Optimized structures of *n*-SW-*m* systems. The gray and white balls denote carbon and hydrogen atoms, respectively. (f) Total energies of the *n*-SW-*m* systems with the energy of 4-SW-4 system as a reference.

Fig. 2 (a-e) Band structures of *n*-SW-*m* systems. Black and red lines denote spin up and down energy bands, respectively. E_g values for the *n*-SW-*m* systems are given below their corresponding band structures. The Fermi level (E_f) is set to zero.

Fig. 3 The band structures of the systems (a) 4-SW-4 under ε = 1.0, 2.5 and 5%; (b) 3-SW-5 under ε = 1.0, 2.0, and 5.0%; (c) 2-SW-6 under ε = 1.2, and 2.0%.

Fig. 4 Charge densities of HOMO-4, HOMO, LUMO and LUMO+4 for 3-SW-5 (a) and 0-SW-8 (c) systems at the Gamma point. The blue and yellow denote positive and negative wave function contours, respectively. The isosurface values are set to be ±0.02 electrons/au^3. (b) Total DOS and PDOS of 3-SW-5 system. Black solid, red and blue dotted lines denote total DOS, PDOS of the edge atoms and the defect site atoms, respectively. (d) HOMO-4, HOMO, LUMO and LUMO+4 for 3-SW-5 with ε = 5.0%. The E_f is set to zero.

Fig. 5 (a-c) Isosurfaces of the spin density distribution ($\Delta\rho = \rho_{up} - \rho_{down}$) for 4-SW-4, 3-SW-5, and 0-SW-8 systems. Dark blue and light orange surfaces correspond to the isosurfaces of up (positive) and down (negative) spin density. The isosurfaces are set to be ±0.005 electrons/au^3.

Fig. 6 Spatial spin density distribution of the 3-SW-5 system under the axis tensile ε of 1.0, 3.0, and 5.0%. The isosurfaces are set to be ±0.005 electrons/au^3.

Fig. 7 Summary of magnetic and electronic phase transitions for the defective 10-ZGNR vs axis tensile ε as SW LD moves from the center to the left edge.

Fig.1

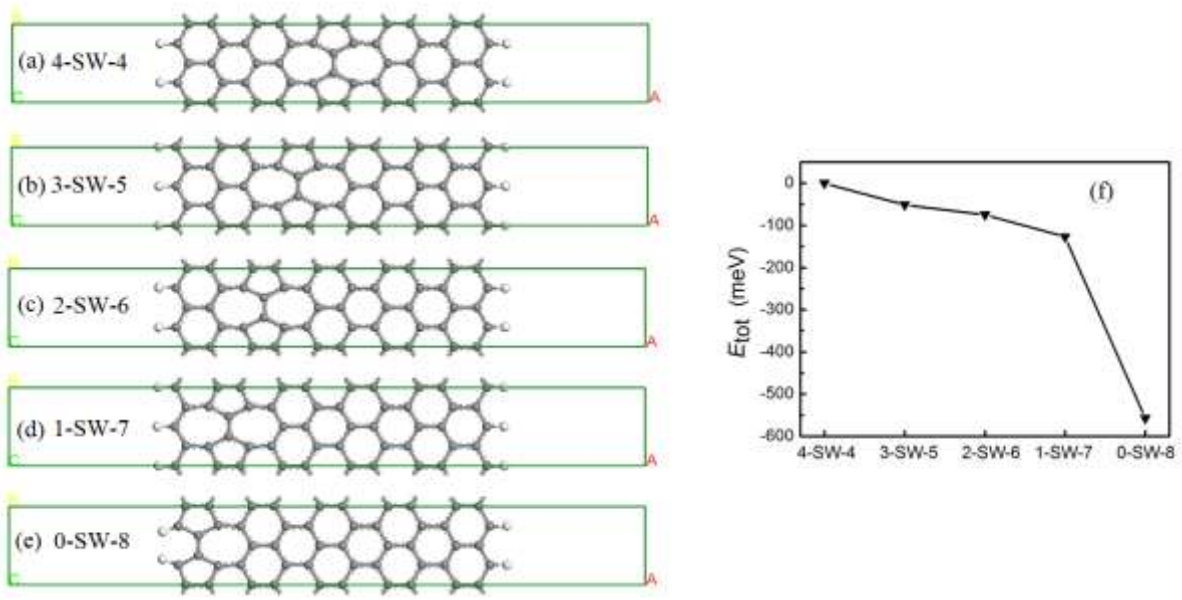

Fig. 2

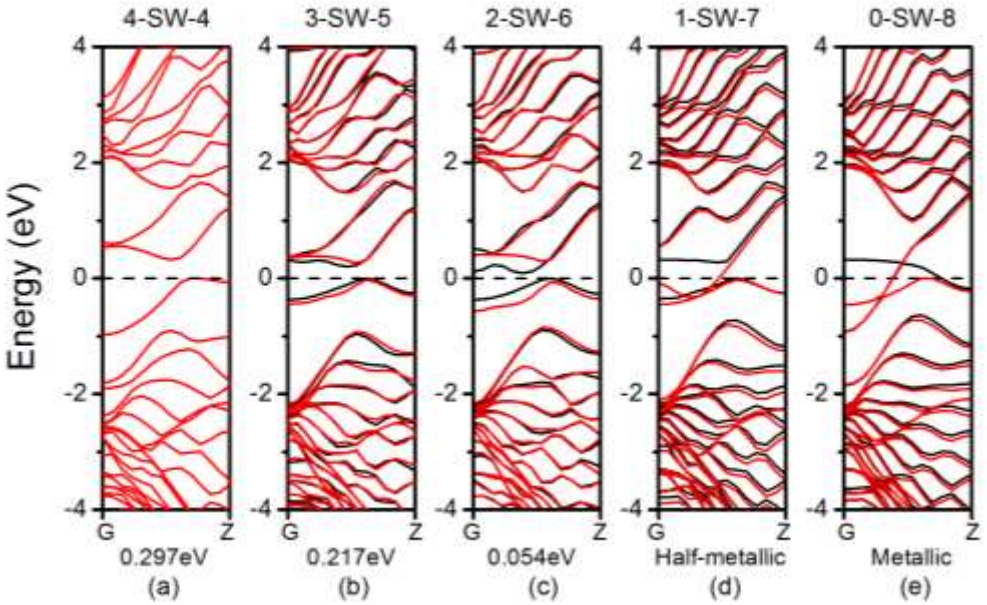

Fig. 3

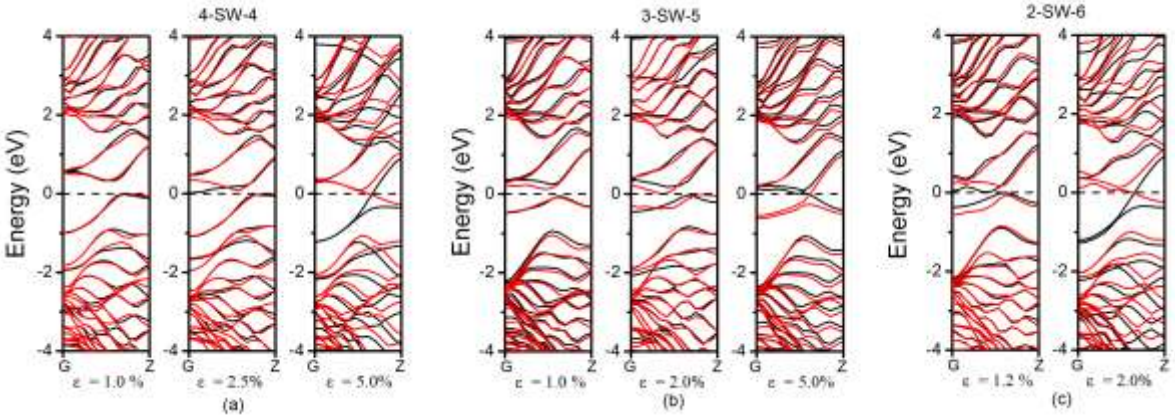

Fig. 4

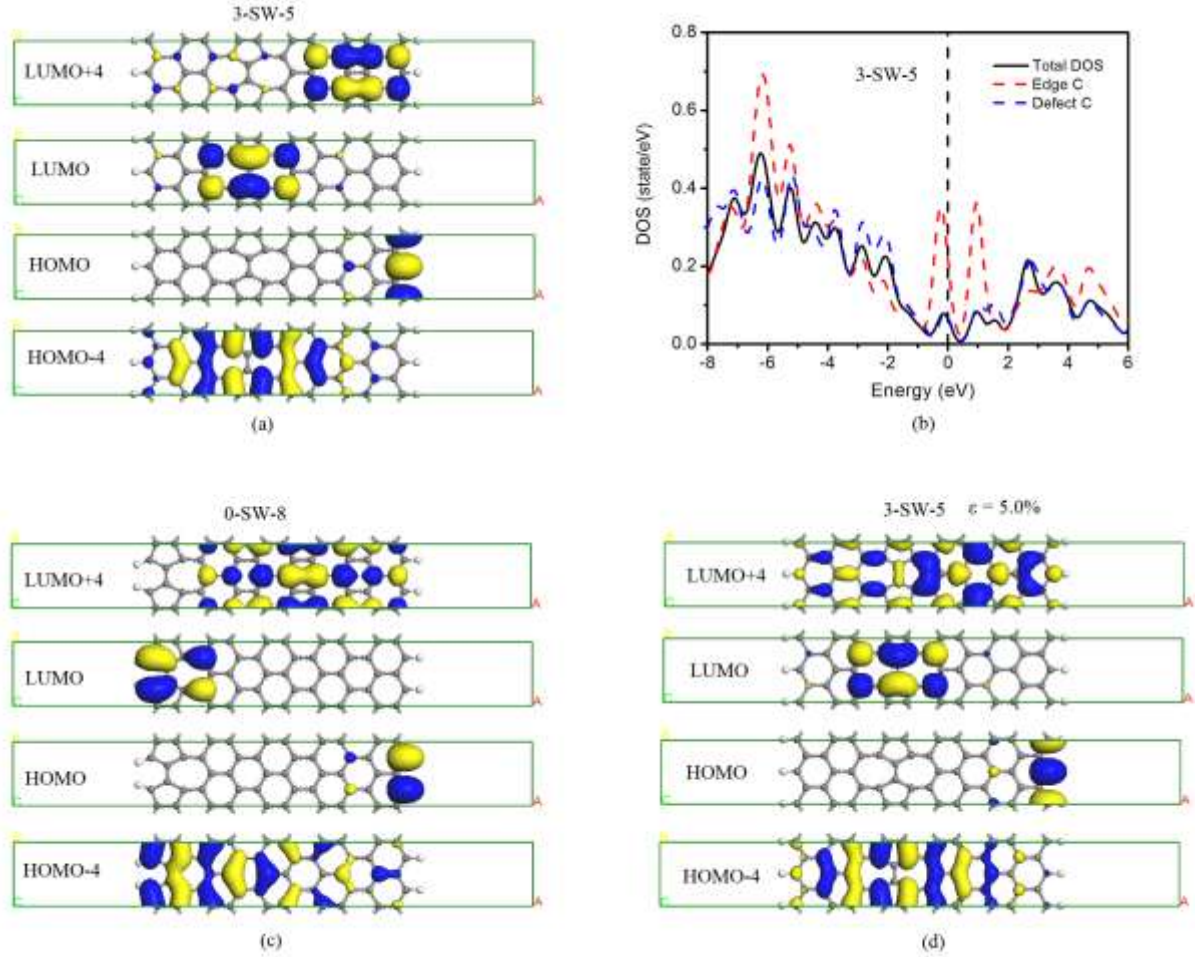

Fig. 5

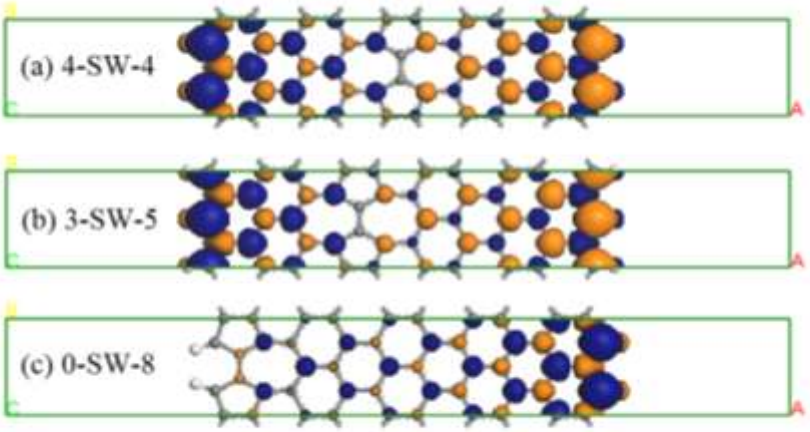

Fig. 6

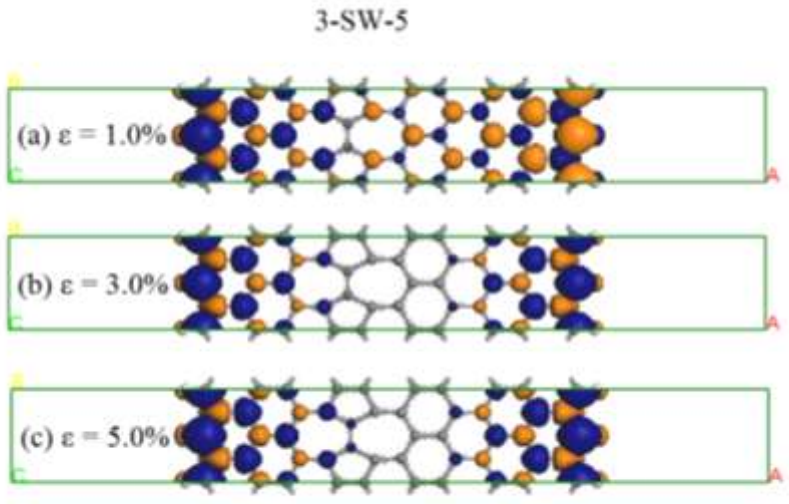

Fig. 7